Letter

Nernst plateau in the quantum limit of low-carrier-density topological insulators

Peng-Lu Zhao [1,2,3] J. L. Zhang,[4,*] Hai-Zhou Lu,[3,2,†] and Qian Niu[1,5]

[1] Department of Physics, University of Science and Technology of China, Hefei, Anhui 230026, China
[2] Quantum Science Center of Guangdong-Hong Kong-Macao Greater Bay Area (Guangdong), Shenzhen 518045, China
[3] State Key Laboratory of Quantum Functional Materials, Department of Physics, and Guangdong Basic Research Center of Excellence for Quantum Science, Southern University of Science and Technology (SUSTech), Shenzhen 518055, China
[4] Anhui Province Key Laboratory of Low-Energy Quantum Materials and Devices, High Magnetic Field Laboratory, HFIPS, Chinese Academy of Sciences, Hefei 230031, China
[5] CAS Key Laboratory of Strongly-Coupled Quantum Matter Physics, University of Science and Technology of China, Hefei, Anhui 230026, China

(Received 22 August 2024; revised 21 July 2025; accepted 1 October 2025; published 22 October 2025)

Nernst effect, a transverse electric current induced by a temperature gradient, is a promising tool for revealing emergent phases of condensed matter. We find a Nernst coefficient plateau in low carrier density topological insulators, as a signature of 1D Weyl points in the quantum limit of the weak topological insulator. The plateau height is inversely proportional to the impurity density, suggesting a way to engineer infinitely large Nernst effects. The Nernst plateau also exists in strong topological insulators, at the bottom of the lowest Landau band. We show that these plateaus have been overlooked in the previous experiments and we highlight the experimental conditions to observe them. Our results may inspire more investigations of employing anomalous Nernst effect to identify emergent phases of condensed matter.

DOI: 10.1103/9tcn-t27z

Introduction. Nernst effect is a thermoelectric Hall effect, exhibiting as a transverse electric current generated by a temperature gradient. It is a promising measurement method to reveal outstanding signatures more than those in the conductivity. Two types of Nernst effects have been observed in the experiments [1,2], the normal one shows a weak-field peak in metals [3–11] and superconductors [10–17] and the anomalous one shows a plateau in topological and magnetic materials in weak fields [18–28] [Fig. 1(a)]. A plateau, quantized or not, is always intriguing, thus the Nernst plateau has attracted significant attention in the past ten years. It can be explained by either the saturation of magnetization or finite Berry curvature induced by the self-rotation of Bloch wave packets [29–32]. Nevertheless, none of these mechanisms applies in strong magnetic fields, where Landau levels are formed and each level produces a quantized Hall conductivity. According to the Mott relation [33–35], both types of the Nernst effect are expected to decay and vanish in extremely strong magnetic fields.

In this Letter, however, we theoretically demonstrate that a Nernst plateau can form in the strong-field quantum limit of topological insulators [Fig. 1(b)], as the ratio of the Nernst coefficient S_{xy} to temperature T,

$$\frac{S_{yx}}{T} = \frac{\pi^2 k_B^2}{3e}\frac{2}{R\Gamma}, \tag{1}$$

where, besides the fundamental constants (the Boltzmann constants k_B, electron charge e, and π), $R = 1$ for weak and $R = 5$ for strong topological insulators, and the Landau-band broadening Γ could remain invariant in the quantum limit, as protected by a detailed charge neutrality resulted from a nontrivial topological phase transition, giving rise to the Nernst plateau. Moreover, the height of this Nernst plateau can increase infinitely with decreasing impurity density. Our results not only predict a Nernst plateau in the ultraquantum limit of low-carrier-density topological insulators, but also suggest a strategy to enhance thermoelectric conversion efficiency.

Landau bands in topological insulators. The 3D strong and weak topological insulators can be generically described by the modified Dirac model [36],

$$H_0(\mathbf{k}) = \hbar v_x k_x \tau_z \sigma_x + \hbar v_y k_y \tau_0 \sigma_y + \hbar v_z k_z \tau_x \sigma_x + \left[\Delta + M_\perp\left(k_x^2 + k_y^2\right) + M_z k_z^2\right]\tau_0\sigma_z, \tag{2}$$

where $v_{x,y,z}$ are the Fermi velocities, and σ and τ are Pauli matrices for pseudo and real spins, respectively. $2|\Delta|$ is the bulk gap, and $M_\perp$ and M_z are two minimal band inversion parameters used to distinguish strong and weak topological insulators [37–42]. Without loss of generality, we assume $\Delta > 0$, then Eq. (2) describes a strong topological insulator when $M_z < M_\perp < 0$ [43–45], a weak topological insulator when $M_\perp < 0$ and $M_z > 0$, or a normal insulator when $M_\perp > 0$ and $M_z > 0$ (see Sec. SI of the Supplemental Material [46]).

By applying a uniform z-direction magnetic field $\mathbf{B} = (0, 0, B)$, the energy spectrum of the topological insulator turns to a series of 1D bands of Landau levels. To analyze the Landau bands (details can be found in Sec. SI of the Supplemental Material [46]), the canonical wave vectors are defined by the Peierls substitution $\mathbf{\Pi} = \boldsymbol{k} + e\boldsymbol{A}/\hbar$ with the Landau gauge potential $\boldsymbol{A} = (-yB, 0, 0)$. The ladder

*Contact author: zhangjinglei@hmfl.ac.cn
†Contact author: luhz@sustech.edu.cn

operators then can be constructed by $\mathbf{\Pi}_x$ and $\mathbf{\Pi}_y$, which further yield the 1D Landau bands as $E^{\mu}_{n\nu}(k_z) = \mu(Z - M_\perp/\ell_B^2) + \nu\sqrt{(M_z k_z^2 + 2M_\perp n/\ell_B^2 + \Delta)^2 + (\sqrt{2n}\hbar v_\perp/\ell_B)^2}$ for $n \geqslant 1$ and $E_{0\nu}(k_z) = \nu|M_z k_z^2 + M_\perp/\ell_B^2 + \Delta - Z|$ for the Lowest Landau bands. Here, μ and ν take values of $\pm$, $v_\perp = \sqrt{v_x v_y}$, $\ell_B = \sqrt{\hbar/eB}$, and $Z = g\mu_B B/2$, where g represents the g-factor and μ_B stands for the Bohr magneton. Z represents the Zeeman energy, as we have included a Zeeman coupling term $H_Z = -g\mu_B B\tau_z\sigma_0/2$ in the free Hamiltonian. The normalized eigenvectors of all Landau bands can be found and are uniformly denoted as $|n\mathbf{k}, +(\nu), +(\mu)\rangle$.

Conductivities and Nernst coefficient. In the strong-field quantum limit where only the lowest Landau bands cross the Fermi energy, the Nernst coefficient can be found according to the Mott relation, which reads

$$S_{xy} = \frac{\pi^2 k_B^2 T}{3e}\frac{\partial \Theta_H}{\partial E_F}, \tag{3}$$

where the Hall angle $\Theta_H \equiv \arctan(\sigma_{xy}/\sigma_{xx})$, the longitudinal, and the Hall conductivities are found by the Kubo-Středa formula [47] at low temperature and in the quantum limit (Sec. SIII of the Supplemental Material [46]) as

$$\sigma_{xx} = \frac{\hbar v_\perp^2 e^2}{2\pi^2\ell_B^2}\int \frac{dk_z}{2\pi}\sum_{\mu,\nu=\pm}\mathcal{A}_{0\mu}\mathcal{T}^{\nu}_{\mu}\mathcal{A}_{1\nu}, \tag{4}$$

$$\sigma_{xy} = \frac{\hbar v_\perp^2 e^2}{2\pi^2\ell_B^2}\int \frac{dk_z}{2\pi}\sum_{\mu,\mu'=\pm}\mathcal{T}^{\nu}_{\mu}(\mathcal{A}_{0\mu}\mathcal{G}_{1\nu} - \mathcal{G}_{0\mu}\mathcal{A}_{1\nu}), \tag{5}$$

where $\mathcal{A}_{0\mu} = \Gamma/[(E_{0\mu} - E_F)^2 + \Gamma^2]$ and $\mathcal{A}_{1\nu} = \Gamma/[(E^{\bar{\mu}}_{1\nu} - E_F)^2 + \Gamma^2]$ represent the spectral functions for the $E_{0\mu}$ and $E^{\bar{\mu}}_{1\nu}$ ($\bar{\mu} = -\mu$) bands, respectively, and $\mathcal{T}^{\nu}_{\mu}$ denotes the transition probability between these two bands. Here, $\mathcal{T}^{\nu}_{\mu}(\mu\nu = +) = [\sin(\theta/2) + \gamma\cos(\theta/2)]^2$ and $\mathcal{T}^{\nu}_{\mu}(\mu\nu = -) = [\cos(\theta/2) - \gamma\sin(\theta/2)]^2$, where $\gamma = \sqrt{2}M_\perp/(\hbar v_\perp \ell_B)$ is a dimensionless parameter, and for $\theta \in (0, \pi)$, $\cos\theta = E_{\mathrm{d}}/\sqrt{E_{\mathrm{d}}^2 + (\sqrt{2}\hbar v_\perp/\ell_B)^2}$ with $E_{\mathrm{d}} = M_z k_z^2 + 2M_\perp/\ell_B^2 + \Delta$. $\mathcal{G}_{0\mu} = [(E_{0\mu} - E_F)^2 - \Gamma^2]/[(E_{0\mu} - E_F)^2 + \Gamma^2]^2$ and $\mathcal{G}_{1\nu} = [(E^{\bar{\mu}}_{1\nu} - E_F)^2 - \Gamma^2]/[(E^{\bar{\mu}}_{1\nu} - E_F)^2 + \Gamma^2]^2$. Equations (4) and (5) are derived under $k_B T \ll \Gamma$ to ensure the Mott relation holds. High temperatures and inelastic electron-phonon scattering can break the Mott relation [33–35]. For $k_B T \ll \Gamma$, phonons are frozen out, inelastic scattering is negligible, and the Mott relation remains valid. Additionally, the quantum limit approximation is well justified when the broadening is much smaller than the Landau band spacing at $k_z = 0$, which for typical topological insulators [37,48,49] is expressed as $\Gamma \ll \sqrt{2}\hbar v_\perp/\ell_B$.

Nernst plateau in weak topological insulators. By substituting the calculated conductivities [Eqs. (4) and (5)] into the Mott relation [Eq. (3)], one can obtain the evolution of S_{xy} with respect to B. For weak topological insulators, we found that S_{xy} forms a field-independent plateau after a critical value ($\gg B_{\mathrm{QL}}$) [see Fig. 2(b)]. This behavior manifests under the stringent condition of an extremely low carrier density.

For a detailed explanation of our findings, we begin by illustrating the evolution of the lowest Landau band with B.

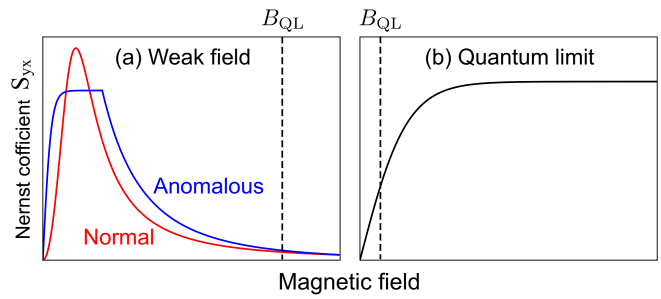

FIG. 1. (a) Schematic of the previously known two types of the Nernst effect, in terms of the dependence of the Nernst coefficient S_{yx} on the magnetic field at a fixed and low temperature T. (b) In comparison, we find a Nernst plateau beyond the expectation of the previous mechanisms, at magnetic fields far above the strong-field quantum limit B_{QL} (indicated by the black dashed lines), where only the lowest Landau band is occupied by electrons.

As shown in Fig. 3(a), the two lowest Landau bands have a gap at the quantum limit for a weak topological insulator ($M_\perp$, $M_z > 0$, and $\Delta > 0$). As B increases, the E_{0+} band shifts downwards while the E_{0-} band shifts upwards. Consequently, the gap between them decreases and closes at $B_1 = \Delta/(-M_\perp e/\hbar + g\mu_B/2)$ [see Fig. 3(b)]. As B increases further to B_2 (see Sec. SV in the Supplemental Material [46] for the calculation of B_2), which is determined by the real root of

$$(g\mu_B - 2M_\perp e/\hbar)B_2^3 - 2\Delta B_2^2 - M_z(\pi h n_0/e)^2 = 0; \tag{6}$$

the E_{0-} band reaches the Fermi energy. Here, the carrier density is given by $n_0 = \int dk_z \sum_{n,\mu}[f(E^{\mu}_{n+}) - (1 - f(E^{\mu}_{n-}))]/4\pi^2\ell_B^2$. Consequently, the Fermi surface in k_z space undergoes a transition from two points to three points, marking a Lifshitz transition [50–52], which is depicted in Fig. 3(c). Figure 3(d) illustrates that with further increase in B, the Fermi energy approaches the Weyl points, forming an ideal 1D Weyl state. Our calculations suggest that such an ideal 1D Weyl state gives rise to the flat S_{xy}.

To calculate $S_{xy}(B)$, we need to know how E_F changes with B. Typically, this can be done by keeping either E_F or the carrier density n_0 constant [53,54]. When assuming n_0 is constant, as shown in Fig. 2(a), the calculated E_F decreases with increasing B before the Lifshitz transition, after which E_F becomes almost field independent. Therefore, S_{xy} is calculated by keeping n_0 constant before the Lifshitz transition and E_F constant after the transition. The results of $S_{xy}(B)$ at $T = 2$ K are plotted in Fig. 2(b), showing that S_{xy} rapidly decays with increasing B before the Lifshitz transition. After the transition, S_{xy} quickly saturates, forming a field-independent plateau. Such a plateau can be analytically obtained as a result of the ideal 1D Weyl state shown in Fig. 3(d). Due to charge neutrality at the Weyl point, $\sigma_{xy} = 0$, and as a result,

$$S_{xy} = \pi^2 k_B^2 T/3e\,\sigma_{xx}^{-1}\partial\sigma_{xy}/\partial E_F. \tag{7}$$

Moreover, Eqs. (4) and (5) in an ideal Weyl state produce (see Sec. SVIA in the Supplemental Material [46])

$$\sigma_{xx} = \frac{e^2}{\pi h}\frac{\Gamma}{2M_z k_w}, \quad \frac{\partial\sigma_{xy}}{\partial E_F} = -\frac{e^2}{\pi h}\frac{1}{M_z k_w}, \tag{8}$$

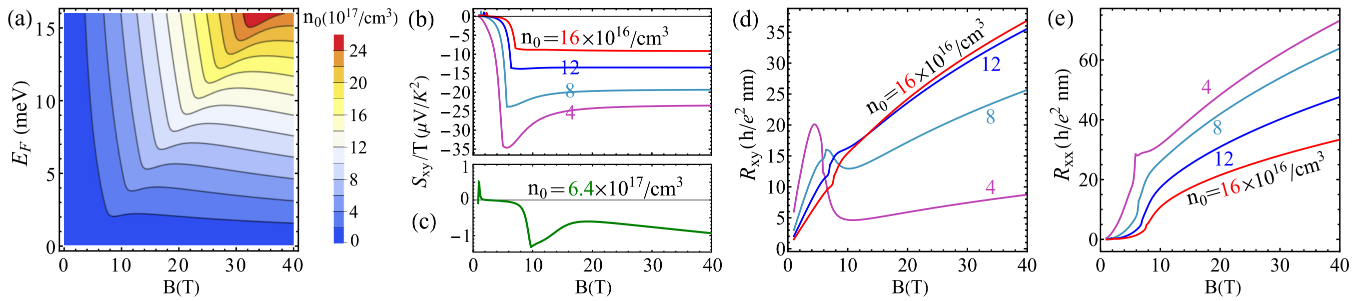

FIG. 2. Computed functions of $E_F(B)$, $S_{xy}(B)$, $R_{yx}(B)$, and $R_{xx}(B)$ for weak topological insulators at $T = 2$ K. (a) Contour plot in the $B - E_F$ plane for a fixed carrier density n_0 of weak topological insulators. Each line represents a constant n_0, and the different colors correspond to varying values of n_0, which are labeled in the right panel. (b), (d), and (e) Calculated $S_{xy}(B)$, $R_{xy}(B)$, and $R_{xx}(B)$, respectively, for different carrier densities labeled by the colored numbers. All plots begin at $B = 1$T—at the quantum limit for $n_0 = 4\times10^{16}/\mathrm{cm}^3$, but at the second Landau band for the other three carrier densities. (c) Calculated $S_{xy}(B)$ with an n_0 higher than those in (b); in this case, S_{xy} does not exhibit a plateau as in (b). This plot begins in the second Landau band at 6 T. In all diagrams, we take $M_\perp = -12\,\mathrm{eV}\cdot$ Å^2, $M_z = 3\mathrm{eV}\cdot$ Å^2, $\Delta = 2.5\,\mathrm{meV}$, $v_\perp = 5\times10^5\mathrm{m/s}$, $g = 12$, and $\Gamma = 2\,\mathrm{meV}$. The quantum limits for $n_0 = (4, 8, 12, 16, 64)\times10^{16}/\mathrm{cm}^3$ are $B_0 = 0.77, 1.32, 1.82, 2.28,$ and 6.81T, respectively.

where $k_w = \sqrt{[(-M_\perp e/\hbar + g\mu_B/2)B - \Delta]/M_z}$ representing the position of the Weyl point. Substituting Eq. (8) into Eq. (7) yields $S_{xy}/T = -2\pi^2 k_B^2/(3e\Gamma)$, which corresponds to $R = 1$ in Eq. (1). Additionally, as shown in Sec. SVIC in the Supplemental Material [46], each subfigure in Fig. 3 leads to a special point in the Nernst coefficient curve shown in Fig. 2(b). Specifically, Fig. 3(a) leads to the peak value of the Nernst coefficient in Fig. 2(b); Fig. 3(b) leads to the point where the Nernst coefficient crosses zero in Fig. 2(b); and Fig. 3(c) leads to the valley value in Fig. 2(b).

The emergence of this plateau is highly sensitive to the carrier density n_0. As shown in Fig. 2(c), when n_0 is increased to be $6.4\times10^{17}/\mathrm{cm}^3$, no plateau appears regardless of the magnitude of B. The main reason is that for such an n_0, the E_F after the Lifshitz transition is relatively high [see Fig. 2(a)], thus far from the ideal Weyl state. For such a case, we have also obtained approximate result of S_{xy}/T under strong magnetic field (see Sec. SVI in the Supplemental Material [46]), which clearly demonstrates the dependence of S_{xy} on B and shows that S_{xy} does not exhibit a plateau in strong magnetic fields. Furthermore, Eq. (6) shows that $B_2 \propto n_0^{2/3}$, and Fig. 2(a) show that as n_0 decreases, the Fermi energy at B_2 is closer to the 1D Weyl point, meaning B_3 decreases with n_0. Therefore, the emergence of a Nernst plateau within experimentally accessible fields requires n_0 to be sufficiently low—a condition independent of specific material details—making our prediction highly universal.

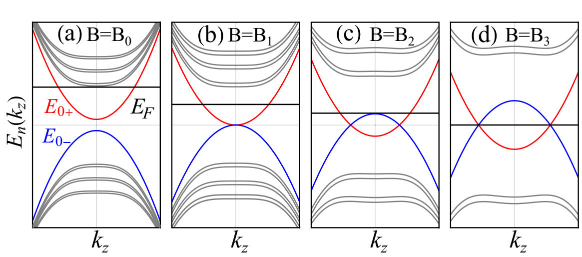

FIG. 3. Evolution of Landau bands with increasing B at several critical values. The red, blue, and gray lines are for the 0th Landau bands E_{0+}, E_{0-} and high-index Landau bands, respectively. The black line represents the Fermi energy E_F. (a) The quantum limit reaches at B_0, where the Fermi energy touches the band bottom of E_{1+}^-. (b) The gap of the 0th Landau band closes at B_1. (c) The Lifshitz transition happens at B_2, where E_F crosses the bottom of E_{0-}. (d) Ideal 1D Weyl states emerge at B_3, with all Weyl points located at E_F.

The experimental phenomenon of the Nernst plateau bears resemblance to that of the anomalous Nernst effect. To distinguish between them, we also computed the behaviors of the corresponding $R_{xy}(B)$ and $R_{xx}(B)$. Figure 2(d) illustrates the variation of R_{xy} with B, showing that R_{xy} does not exhibit a plateau. This is a significant distinction between our results and the experimental phenomenon of anomalous Nernst effect, as the plateau in anomalous Nernst effect typically accompanies the anomalous Hall plateau [2,20,55]. Furthermore, Eq. (8) indicates that when the S_{xy} plateau appears, R_{xx} increases with B according to $\sqrt{(-M_\perp e/\hbar + g\mu_B/2)B - \Delta}$, as shown in Fig. 2(e). Observing such behaviors of R_{xx} in experiments provides additional support for validating our plateau theory.

Nernst plateau in strong topological insulators. We will demonstrate that the flat Nernst effect obtained in weak topological insulators also emerges in strong topological insulators [see Fig. 4(b)], albeit requiring lower carrier concentrations and involving distinct mechanisms. First, as shown in Fig. 5, the evolution of Landau bands in strong topological insulators behaves exactly opposite to that depicted in Fig. 3 for weak topological insulators. For strong topological insulators ($M_z < M_\perp < 0$, and $\Delta > 0$), the Weyl points formed by E_{0+} and E_{0-} are present in weak magnetic fields [see Fig. 5(a)]. As B increases, E_{0+} moves upward, and E_{0-} moves downward. When reaching B_1, the two Weyl points merge into one, as shown in Fig. 5(b). Figure 5(c) illustrates that with a further increase in B, a gap of size $2(-M_\perp e/\hbar + g\mu_B/2)(B - B_1)$ opens between the two 0th Landau bands.

When calculating $S_{xy}(B)$ for strong topological insulators, we always keep the carrier density n_0 constant. If we keep E_F constant, the system will quickly become insulating with increasing B because the E_{0+} band moves upward and the E_{0-} band moves downward. With n_0 being constant, as shown in Fig. 4(a), the calculated E_F first decreases and then increases almost linearly as B increases. Using the calculated $E_F(B)$

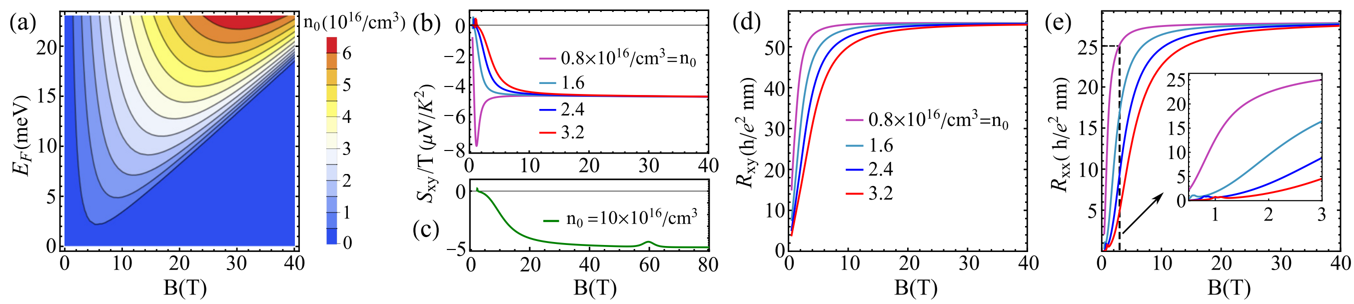

FIG. 4. Computed functions of $E_F(B)$, $S_{xy}(B)$, $R_{yx}(B)$, and $R_{xx}(B)$ for strong topological insulators at $T = 2\,\mathrm{K}$. (a) Contour plot in the $B - E_F$ plane for a fixed carrier density n_0 of strong topological insulators. (b), (d), and (e) Calculated $S_{xy}(B)$, $R_{xy}(B)$, and $R_{xx}(B)$, respectively, for different carrier densities labeled by the colored numbers. All plots begin at $B = 0.5\,\mathrm{T}$—at the quantum limit for $n_0 = 0.8\times10^{16}/\mathrm{cm}^3$, but at the second Landau band for the other three carrier densities. The inset in (e) plotted $R_{xx}(B)$ for $B \in (0.5, 3)\,\mathrm{T}$, and the labels for the lines in (e) are the same as those in (d). (c) Calculated $S_{xy}(B)$ with an n_0 higher than those in (b); in this case, S_{xy} is not flat even for $B \sim 100\,\mathrm{T}$. This plot begins in the second Landau band at 3 T. For all diagrams, we take $M_\perp = -120\,\mathrm{eV}\cdot\mathrm{Å}^2$, $M_z = -12\mathrm{eV}\cdot\mathrm{Å}^2$. The values of Δ, $v_\perp$, g, and Γ are the same as those used in Fig. 2. The quantum limits for $n = (0.8, 1.6, 2.4, 3.2, 10)\times10^{16}/\mathrm{cm}^3$ are $B_0 = 0.34, 0.61, 0.86, 1.11$, and $3.11\,\mathrm{T}$, respectively.

to compute the $S_{xy}(B)$ yields the results shown in Fig. 4(b). Clearly, $S_{xy}(B)$ also flattens in strong magnetic fields. Compared to the case of weak topological insulators shown in Fig. 2(b), the carrier density here is nearly an order of magnitude lower, and while the Nernst plateau values vary with carrier density in weak topological insulators, they remain constant in this case. The flat S_{xy} appearing here can be understood as the effect of the band bottom shown in Fig. 5(c), which is completely different from the ideal Weyl state in the case of weak topological insulators. Near the band bottom, σ_{xy} is comparable to σ_{xx}. To obtain the approximate results of the Nernst coefficient, we need to calculate the asymptotic results of σ_{xy}, σ_{xx}, $\partial\sigma_{xy}/\partial E_F$, and $\partial\sigma_{xx}/\partial E_F$ separately. The detailed calculations are presented in Sec. SVIB in the Supplemental Material [46], and the approximate results are as follows:

$$\sigma_{xx} = \frac{e^2}{\pi h}\frac{\sqrt{\Gamma}}{4\sqrt{2|M_z|}}, \qquad \frac{\partial\sigma_{xx}}{\partial E_F} = \frac{e^2}{\pi h}\frac{1}{8\sqrt{2|M_z|\Gamma}}, \tag{9}$$

$$\sigma_{xy} = -\frac{e^2}{\pi h}\frac{\sqrt{\Gamma}}{2\sqrt{2|M_z|}}, \qquad \frac{\partial\sigma_{xy}}{\partial E_F} = -\frac{e^2}{\pi h}\frac{3}{4\sqrt{2|M_z|\Gamma}}. \tag{10}$$

The asymptotic value of the Nernst coefficient is $S_{xy}/T = -2\pi^2 k_B^2/(15e\Gamma)$, i.e., the result for $R = 5$ in Eq. (1), which exactly gives the value of the plateau in Fig. 4(b) when $\Gamma = 2\,\mathrm{meV}$. Experimentally observing the plateau requires a low density. As shown in Fig. 4(c), when $n = 6.4\times10^{16}/\mathrm{cm}^3$, no plateau appears even at magnetic fields as high as 80 T, a value exceeding the limit of steady magnetic fields achievable in current experiments.

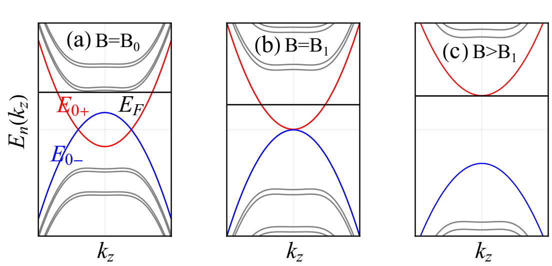

FIG. 5. Evolution of Landau bands for a strong topological insulator under selected magnetic fields. The labels of the lines are the same as those in Fig. 3. (a) The quantum limit reaches at B_0. (b) Two Weyl points merge into one at B_1. (c) The gap between two 0th Landau bands opens after B_1, and as B increases, E_F gradually pushes to the band bottom.

To distinguish the flat Nernst effect in strong topological insulators from the case in weak topological insulators and the anomalous Nernst behavior, we calculated $R_{xy}(B)$ and $R_{xx}(B)$, which are shown in Figs. 4(d) and 4(e), respectively. Clearly, $R_{xy}(B)$ and $R_{xx}(B)$ also become flat under strong magnetic fields, and the values of the plateaus can be obtained through σ_{xx} and σ_{xy} in Eqs. (9) and (10), respectively. Simultaneous saturation of $R_{xy}(B)$ and $R_{xx}(B)$ is rare in topological insulators but was recently observed in $ZrTe_5$ [56,57].

Experimental observations. So far, only a few experiments have observed the Nernst plateau in the quantum limit. Recent experiments in $HfTe_5$ [58] have observed Nernst plateaus in magnetic fields ranging from 15 T to 32 T ($B_{\mathrm{QL}} \sim 1.5\,\mathrm{T}$), and the measured R_{xx} fits well with $\sqrt{B}$ when the Nernst plateau appears. Given that recent infrared magneto-optical experiments have identified $HfTe_5$ as a weak topological insulator [42], and that our model Eq. (2) and the parameters in Fig. 2 also apply to $HfTe_5$, we believe that the experimental results in [58] support our Nernst plateau theory for weak topological insulators. For the case of strong topological insulators, we think that the Nernst plateau observed earlier in $ZrTe_5$ [59] can be explained by our theory. First, our model Eq. (2) and the parameters in Fig. 4 apply to $ZrTe_5$ [38,60]. Second, the carrier density (hole) is very low, leading to $B_{\mathrm{QL}} \sim 0.3\,\mathrm{T}$ [59,61,62], while the observed Nernst plateau appears in the 3–6 T range, which is well beyond the quantum limit.

We anticipate that more experiments reporting this phenomenon in other typical topological insulators such as Bi_2Se_3, Bi_2Te_3, and Sb_2Te_3[37,48,49]. For these materials, the Hamiltonian includes an additional term, $(C + D_z k_z^2 + D_\perp k_\perp^2)\mathrm{I}_{4\times4}$. This term breaks the electron-hole symmetry, resulting in different masses for the lowest electron and hole Landau bands, but does not affect the existence of the Nernst plateau given by Eq. (1) (see Sec. SVIII in the Supplemental Material [46]). However, the challenge in observing the Nernst plateau in these materials is engineering a sufficiently low n_0.

Discussion. In our calculations, we assumed Γ to be field independent, as supported by previous studies [63–66]. Since the Nernst plateau value is proportional to $1/\Gamma$, we confirmed Γ remains field independent by calculating it using the Born approximation with Gaussian disorder [67–70]. Details are in Sec. SVII in the Supplemental Material [46]. The results show that both strong and weak topological insulators can have a field-independent Γ when the Nernst plateau appears. The Nernst plateau value is approximately inversely proportional to impurity density. Reducing the impurity density allows the Nernst plateau value predicted by our theory to surpass the current record, albeit constrained by an upper limit (see Sec. SVIIC in the Supplemental Material [46]), thereby significantly improving thermoelectric conversion efficiency.

Acknowledgments. We thank Yang Gao, Jian-hui Zhou, Zhi Wang, and Song-bo Zhang for fruitful discussions. The work is supported by the National Key R&D Program of China (Grants No. 2023YFA1406300, No. 2022YFA1403700, and No. 2022YFA1602602), the National Natural Science Foundation of China (Grants No. 12304074, No. 12234017, No. 12374041, No. 12525401, No. 12474053, and No. 12350402), Guangdong Basic and Applied Basic Research Foundation (Grant No. 2023B0303000011), Guangdong Provincial Quantum Science Strategic Initiative (Grants No. GDZX2201001 and No. GDZX2401001), the Science, Technology, and Innovation Commission of Shenzhen Municipality (Grant No. ZDSYS20190902092905285), High-level Special Funds (Grant No. G03050K004), and the New Cornerstone Science Foundation through the XPLORER PRIZE. The Basic Research Program of the Chinese Academy of Sciences Based on Major Scientific Infrastructures (Grant No. JZHKYPT-2021-08). The numerical calculations were supported by the Center for Computational Science and Engineering of SUSTech.

Data availability. No data were created or analyzed in this study.

[1] K. Behnia, The Nernst effect and the boundaries of the Fermi liquid picture, J. Phys.: Condens. Matter **21**, 113101 (2009).

[2] K. Behnia and H. Aubin, Nernst effect in metals and superconductors: A review of concepts and experiments, Rep. Prog. Phys. **79**, 046502 (2016).

[3] J. H. Mangez, J. P. Issi, and J. Heremans, Transport properties of bismuth in quantizing magnetic fields, Phys. Rev. B **14**, 4381 (1976).

[4] P. Li and R. L. Greene, Normal-state Nernst effect in electron-doped $Pr_{2-x}Ce_xCuO_{4-\delta}$: Superconducting fluctuations and two-band transport, Phys. Rev. B **76**, 174512 (2007).

[5] R. Bel, K. Behnia, and H. Berger, Ambipolar Nernst effect in $NbSe_2$, Phys. Rev. Lett. **91**, 066602 (2003).

[6] E. S. Choi, J. S. Brooks, H. Kang, Y. J. Jo, and W. Kang, Resonant Nernst effect in the metallic and field-induced spin density wave states of $(TMTSF)_2ClO_4$, Phys. Rev. Lett. **95**, 187001 (2005).

[7] A. Pourret, K. Behnia, D. Kikuchi, Y. Aoki, H. Sugawara, and H. Sato, Drastic change in transport of entropy with quadrupolar ordering in $PrFe_4P_{12}$, Phys. Rev. Lett. **96**, 176402 (2006).

[8] Y. Kasahara, T. Iwasawa, H. Shishido, T. Shibauchi, K. Behnia, Y. Haga, T. D. Matsuda, Y. Onuki, M. Sigrist, and Y. Matsuda, Exotic superconducting properties in the electron-hole-compensated heavy-fermion "semimetal" URu_2Si_2, Phys. Rev. Lett. **99**, 116402 (2007).

[9] K. Behnia, M.-A. Méasson, and Y. Kopelevich, Nernst effect in semimetals: The effective mass and the figure of merit, Phys. Rev. Lett. **98**, 076603 (2007).

[10] P. Spathis, H. Aubin, A. Pourret, and K. Behnia, Nernst effect in the phase-fluctuating superconductor InO_x, Europhys. Lett. **83**, 57005 (2008).

[11] A. Pourret, H. Aubin, J. Lesueur, C. A. Marrache-Kikuchi, L. Bergé, L. Dumoulin, and K. Behnia, Length scale for the superconducting Nernst signal above T_c in $Nb_{0.15}Si_{0.85}$, Phys. Rev. B **76**, 214504 (2007).

[12] R. P. Huebener and A. Seher, Nernst effect and flux flow in superconductors. II. Lead films, Phys. Rev. **181**, 710 (1969).

[13] A. Pourret, H. Aubin, J. Lesueur, C. A. Marrache-Kikuchi, L. Bergé, L. Dumoulin, and K. Behnia, Observation of the nernst signal generated by fluctuating Cooper pairs, Nat. Phys. **2**, 683 (2006).

[14] F. F. Tafti, F. Laliberté, M. Dion, J. Gaudet, P. Fournier, and L. Taillefer, Nernst effect in the electron-doped cuprate superconductor $Pr_{2-x}Ce_xCuO_4$: Superconducting fluctuations, upper critical field H_{c2}, and the origin of the T_c dome, Phys. Rev. B **90**, 024519 (2014).

[15] J. Chang, N. Doiron-Leyraud, O. Cyr-Choinière, G. Grissonnanche, F. Laliberté, E. Hassinger, J.-P. Reid, R. Daou, S. Pyon, T. Takayama, H. Takagi, and L. Taillefer, Decrease of upper critical field with underdoping in cuprate superconductors, Nat. Phys. **8**, 751 (2012).

[16] Z. A. Xu, N. P. Ong, Y. Wang, T. Kakeshita, and S. Uchida, Vortex-like excitations and the onset of superconducting phase fluctuation in underdoped $La_{2-x}Sr_xCuO_4$, Nature (London) **406**, 486 (2000).

[17] Y. Wang, L. Li, and N. P. Ong, Nernst effect in high-T_c superconductors, Phys. Rev. B **73**, 024510 (2006).

[18] W. L. Lee, S. Watauchi, V. L. Miller, R. J. Cava, and N. P. Ong, Anomalous Hall heat current and Nernst effect in the $CuCr_2Se_{4-x}Br_x$ ferromagnet, Phys. Rev. Lett. **93**, 226601 (2004).

[19] T. Miyasato, N. Abe, T. Fujii, A. Asamitsu, S. Onoda, Y. Onose, N. Nagaosa, and Y. Tokura, Crossover behavior of the anomalous Hall effect and anomalous Nernst effect in itinerant ferromagnets, Phys. Rev. Lett. **99**, 086602 (2007).

[20] Y. Pu, D. Chiba, F. Matsukura, H. Ohno, and J. Shi, Mott relation for anomalous Hall and Nernst effects in $Ga_{1-x}Mn_xAs$ ferromagnetic semiconductors, Phys. Rev. Lett. **101**, 117208 (2008).

[21] M. Ikhlas, T. Tomita, T. Koretsune, M. T. Suzuki, D. Nishio-Hamane, R. Arita, Y. Otani, and S. Nakatsuji, Large anomalous Nernst effect at room temperature in a chiral antiferromagnet, Nat. Phys. **13**, 1085 (2017).

[22] X. Li, L. Xu, L. Ding, J. Wang, M. Shen, X. Lu, Z. Zhu, and K. Behnia, Anomalous Nernst and righi-leduc effects in Mn_3Sn:

Berry curvature and entropy flow, Phys. Rev. Lett. **119**, 056601 (2017).
[23] X. Li, L. Xu, H. Zuo, A. Subedi, Z. Zhu, and K. Behnia, Momentum-space and real-space Berry curvatures in Mn_3Sn, SciPost Phys. **5**, 063 (2018).
[24] A. Sakai, Y. P. Mizuta, A. A. Nugroho, R. Sihombing, T. Koretsune, M. T. Suzuki, N. Takemori, R. Ishii, D. Nishio-Hamane, R. Arita, P. Goswami, and S. Nakatsuji, Giant anomalous Nernst effect and quantum-critical scaling in a ferromagnetic semimetal, Nat. Phys. **14**, 1119 (2018).
[25] S. N. Guin, P. Vir, Y. Zhang, N. Kumar, S. J. Watzman, C. Fu, E. Liu, K. Manna, W. Schnelle, J. Gooth, C. Shekhar, Y. Sun, and C. Felser, Zero-field Nernst effect in a ferromagnetic kagome-lattice Weyl-semimetal $Co_3Sn_2S_2$, Adv. Mater. **31**, 1806622 (2019).
[26] L. Xu, X. Li, X. Lu, C. Collignon, H. Fu, J. Koo, B. Fauqué, B. Yan, Z. Zhu, and K. Behnia, Finite-temperature violation of the anomalous transverse Wiedemann-Franz law, Sci. Adv. **6**, eaaz3522 (2020).
[27] H. Yang, W. You, J. Wang, J. Huang, C. Xi, X. Xu, C. Cao, M. Tian, Z. A. Xu, J. Dai, and Y. Li, Giant anomalous Nernst effect in the magnetic Weyl semimetal $Co_3Sn_2S_2$, Phys. Rev. Mater. **4**, 024202 (2020).
[28] C. Wuttke, F. Caglieris, S. Sykora, F. Scaravaggi, A. U. Wolter, K. Manna, V. Süss, C. Shekhar, C. Felser, B. Büchner, and C. Hess, Berry curvature unravelled by the anomalous Nernst effect in Mn_3Ge, Phys. Rev. B **100**, 085111 (2019).
[29] M.-C. Chang and Q. Niu, Berry phase, hyperorbits, and the Hofstadter spectrum, Phys. Rev. Lett. **75**, 1348 (1995).
[30] M.-C. Chang and Q. Niu, Berry phase, hyperorbits, and the Hofstadter spectrum: Semiclassical dynamics in magnetic Bloch bands, Phys. Rev. B **53**, 7010 (1996).
[31] G. Sundaram and Q. Niu, Wave-packet dynamics in slowly perturbed crystals: Gradient corrections and Berry-phase effects, Phys. Rev. B **59**, 14915 (1999).
[32] D. Xiao, M. C. Chang, and Q. Niu, Berry phase effects on electronic properties, Rev. Mod. Phys. **82**, 1959 (2010).
[33] L. Smrcka and P. Stŗeda, Transport coefficients in strong magnetic fields, J. Phys. C: Solid State Phys. **10**, 2153 (1977).
[34] M. Jonson and G. D. Mahan, Mott's formula for the thermopower and the Wiedemann-Franz law, Phys. Rev. B **21**, 4223 (1980).
[35] M. Jonson and S. M. Girvin, Thermoelectric effect in a weakly disordered inversion layer subject to a quantizing magnetic field, Phys. Rev. B **29**, 1939 (1984).
[36] S.-Q. Shen, *Topological Insulators*, 2nd ed. (Springer-Verlag, Berlin, Heidelberg, 2017).
[37] H. Zhang, C.-X. Liu, X.-L. Qi, X. Dai, Z. Fang, and S.-C. Zhang, Topological insulators in Bi_2Se_3, Bi_2Te_3 and Sb_2Te_3 with a single Dirac cone on the surface, Nat. Phys. **5**, 438 (2009).
[38] R. Y. Chen, Z. G. Chen, X.-Y. Song, J. A. Schneeloch, G. D. Gu, F. Wang, and N. L. Wang, Magnetoinfrared spectroscopy of Landau levels and Zeeman splitting of three-dimensional massless Dirac fermions in $ZrTe_5$, Phys. Rev. Lett. **115**, 176404 (2015).
[39] J. L. Zhang, C. M. Wang, C. Y. Guo, X. D. Zhu, Y. Zhang, J. Y. Yang, Y. Q. Wang, Z. Qu, L. Pi, H. Z. Lu, and M. L. Tian, Anomalous thermoelectric effects of $ZrTe_5$ in and beyond the quantum limit, Phys. Rev. Lett. **123**, 196602 (2019).
[40] E. Martino, I. Crassee, G. Eguchi, D. Santos-Cottin, R. D. Zhong, G. D. Gu, H. Berger, Z. Rukelj, M. Orlita, C. C. Homes, and A. Akrap, Two-dimensional conical dispersion in $ZrTe_5$ evidenced by optical spectroscopy, Phys. Rev. Lett. **122**, 217402 (2019).
[41] Y. Jiang, J. Wang, T. Zhao, Z. L. Dun, Q. Huang, X. S. Wu, M. Mourigal, H. D. Zhou, W. Pan, M. Ozerov, D. Smirnov, and Z. Jiang, Unraveling the topological phase of $ZrTe_5$ via magnetoinfrared spectroscopy, Phys. Rev. Lett. **125**, 046403 (2020).
[42] W. Wu, Z. Shi, Y. Du, Y. Wang, F. Qin, X. Meng, B. Liu, Y. Ma, Z. Yan, M. Ozerov, C. Zhang, H.-Z. Lu, J. Chu, and X. Yuan, Topological Lifshitz transition and one-dimensional Weyl mode in $HfTe_5$, Nat. Mater. **22**, 84 (2023).
[43] L. Fu, C. L. Kane, and E. J. Mele, Topological insulators in three dimensions, Phys. Rev. Lett. **98**, 106803 (2007).
[44] L. Fu and C. L. Kane, Topological insulators with inversion symmetry, Phys. Rev. B **76**, 045302 (2007).
[45] B. Yan, L. Müchler, and C. Felser, Prediction of weak topological insulators in layered semiconductors, Phys. Rev. Lett. **109**, 116406 (2012).
[46] See Supplemental Material at http://link.aps.org/supplemental/10.1103/9tcn-t27z for detailed calculations, which also includes Refs. [33–45,47–49,53,54,67–70].
[47] P. Streda, Theory of quantised Hall conductivity in two dimensions, J. Phys. C **15**, L717 (1982).
[48] X.-L. Qi and S.-C. Zhang, Topological insulators and superconductors, Rev. Mod. Phys. **83**, 1057 (2011).
[49] H.-Z. Lu, W.-Y. Shan, W. Yao, Q. Niu, and S.-Q. Shen, Massive Dirac fermions and spin physics in an ultrathin film of topological insulator, Phys. Rev. B **81**, 115407 (2010).
[50] A. A. Varlamov and A. V. Pantsulaya, Anomalous kinetic properties of metals near the Lifshitz topological transition, Zh. Eksp. Teor. Fiz. **89**, 2188 (1985).
[51] A. A. Varlamov, V. S. Egorov, and A. V. Pantsulaya, Kinetic properties of metals near electronic topological transitions (2 1/2-order transitions), Adv. Phys. **38**, 469 (1989).
[52] Y. Blanter, M. Kaganov, A. Pantsulaya, and A. Varlamov, The theory of electronic topological transitions, Phys. Rep. **245**, 159 (1994).
[53] G. D. Mahan, *Many Particle Physics*, 3rd ed. (Plenum, New York, 2000).
[54] C.-L. Zhang, C. M. Wang, Z. Yuan, X. Xu, G. Wang, C.-C. Lee, L. Pi, C. Xi, H. Lin, N. Harrison, H.-Z. Lu, J. Zhang, and S. Jia, Non-saturating quantum magnetization in weyl semimetal taas, Nat. Commun. **10**, 1028 (2019).
[55] D. Xiao, Y. Yao, Z. Fang, and Q. Niu, Berry-phase effect in anomalous thermoelectric transport, Phys. Rev. Lett. **97**, 026603 (2006).
[56] A. Gourgout, M. Leroux, J. L. Smirr, M. Massoudzadegan, R. P. Lobo, D. Vignolles, C. Proust, H. Berger, Q. Li, G. Gu, C. C. Homes, A. Akrap, and B. Fauqué, Magnetic freeze-out and anomalous Hall effect in $ZrTe_5$, npj Quantum Mater. **7**, 71 (2022).
[57] P.-J. Shih, C.-H. Yang, P.-C. Liao, W.-C. Lin, F.-H. Chen, J.-C. Chen, L. Cao, C. Chuang, and C.-T. Liang, Unveiling the phases of bulk $ZrTe_5$ through magnetotransport phenomena, Nanotechnology **36**, 095204 (2025).

[58] Y. Zhang, Q. Li, P. Zhao, Y. Qian, Y. Lv, Y. Chen, Q. Niu, H. Lu, J. Zhang, and M. Tian, Observation of giant Nernst plateau in ideal 1D Weyl phase, arXiv:2410.11154.

[59] T. Liang, J. Lin, Q. Gibson, S. Kushwaha, M. Liu, W. Wang, H. Xiong, J. A. Sobota, M. Hashimoto, P. S. Kirchmann, Z. X. Shen, R. J. Cava, and N. P. Ong, Anomalous Hall effect in $ZrTe_5$, Nat. Phys. **14**, 451 (2018).

[60] F. Tang, Y. Ren, P. Wang, R. Zhong, J. Schneeloch, S. A. Yang, K. Yang, P. A. Lee, G. Gu, Z. Qiao, and L. Zhang, Three-dimensional quantum Hall effect and metal-insulator transition in $ZrTe_5$, Nature (London) **569**, 537 (2019).

[61] H. Wang, H. Liu, Y. Li, Y. Liu, J. Wang, J. Liu, J. Y. Dai, Y. Wang, L. Li, J. Yan, D. Mandrus, X. C. Xie, and J. Wang, Discovery of log-periodic oscillations in ultraquantum topological materials, Sci. Adv. **4**, eaau5096 (2018).

[62] P. Shahi, D. J. Singh, J. P. Sun, L. X. Zhao, G. F. Chen, Y. Y. Lv, J. Li, J.-Q. Yan, D. G. Mandrus, and J.-G. Cheng, Bipolar conduction as the possible origin of the electronic transition in pentatellurides: Metallic vs semiconducting behavior, Phys. Rev. X **8**, 021055 (2018).

[63] E. Gornik, R. Lassnig, G. Strasser, H. L. Störmer, A. C. Gossard, and W. Wiegmann, Specific heat of two-dimensional electrons in Gaas-Gaalas multilayers, Phys. Rev. Lett. **54**, 1820 (1985).

[64] T. P. Smith, B. B. Goldberg, P. J. Stiles, and M. Heiblum, Direct measurement of the density of states of a two-dimensional electron gas, Phys. Rev. B **32**, 2696 (1985).

[65] R. Ashoori and R. Silsbee, The Landau level density of states as a function of Fermi energy in the two dimensional electron gas, Solid State Commun. **81**, 821 (1992).

[66] C. Wang, Thermodynamically induced transport anomaly in dilute metals $ZrTe_5$ and $HfTe_5$, Phys. Rev. Lett. **126**, 126601 (2021).

[67] A. A. Abrikosov, Quantum magnetoresistance, Phys. Rev. B **58**, 2788 (1998).

[68] H.-Z. Lu, S.-B. Zhang, and S.-Q. Shen, High-field magnetoconductivity of topological semimetals with short-range potential, Phys. Rev. B **92**, 045203 (2015).

[69] H.-Z. Lu and S.-Q. Shen, Weak antilocalization and localization in disordered and interacting Weyl semimetals, Phys. Rev. B **92**, 035203 (2015).

[70] S.-B. Zhang, H.-Z. Lu, and S.-Q. Shen, Linear magnetoconductivity in an intrinsic topological Weyl semimetal, New J. Phys. **18**, 053039 (2016).